RSC Advances

PAPER

View Article Online
View Journal | View Issue

Cite this: *RSC Adv.*, 2025, **15**, 36808

Synthesis and evaluation of a camphorquinone-derived BTP for minor actinide separation from acidic high-level radioactive liquid waste

Kumari Anshul,[ab] Selvakumar Jayaprakasam,*[ab] Suneel Gattu,[b] Subramanian Srinivasan[b] and G. Srinivasa Rao[b]

Received 21st July 2025
Accepted 26th September 2025

DOI: 10.1039/d5ra05245a

rsc.li/rsc-advances

A camphorquinone-derived bis-triazinylpyridine, bis-2,6-(5,6,7,8-tetrahydro-5,9,9-trimethyl-5,8-methano-1,2,4-benzotriazin-3-yl)pyridine (CA-BTP), was synthesised and systematically evaluated for the selective separation of minor actinides (MA: ^{241}Am and ^{154}Eu) from acidic high-level radioactive liquid waste (HLW). The extractant was purified by gradient polarity chromatography, with structure confirmation *via* FT-IR, ^{1}H NMR, ESI-MS, and TG-DSC, affirming chemical purity and thermal robustness. Extraction studies revealed excellent solubility and stability in 1-octanol and isodecyl alcohol (IDA), with sharp phase separation and no third-phase formation. Radiotracer experiments using ^{241}Am and ^{154}Eu demonstrated high selectivity, achieving separation factors ($SF_{Am/Eu}$) of 150–280 at 1 M HNO_3 using 0.1 M CA-BTP. Mechanistic investigations included acid uptake, nitrate ion dependence, temperature variation, and slope analysis, revealing a 3 : 1 ligand-to-metal stoichiometry and an exothermic extraction process ($\Delta H = -33.6$ to -42.5 kJ mol^{-1}). CA-BTP also showed efficient back-extraction under mild acidic conditions (0.01 M HNO_3), without the need for synergists or complexing agents. These findings position CA-BTP as a robust, scalable, and selective extractant for advanced SANEX-type flowsheets aimed at minor actinide partitioning from chemically similar lanthanides.

1. Introduction

Minor actinides (MA), such as americium (Am(III)) and curium (Cm(III)), are key contributors to the long-term radiotoxicity and decay heat of high-level radioactive waste (HLW), particularly after the decay of shorter-lived fission products like cesium-137 and strontium-90.[1–4] Their presence necessitates geological disposal with prolonged institutional control spanning thousands of years. The selective separation and recovery of these minor actinides from HLW can significantly reduce the radiotoxic lifetime of nuclear waste, potentially shortening the required isolation period from millennia to a few hundred years.[5] Additionally, the partitioned MAs can be recycled or transmuted in fast reactors, supporting a closed nuclear fuel cycle and reducing the long-term burden of nuclear waste management.[6]

However, a major scientific and operational challenge lies in separating MAs from trivalent lanthanides (Ln), which are present in 10–50 times higher concentrations, depending on the burnup and cooling period of spent fuel. While chemically similar to actinides, these lanthanides interfere with the transmutation process due to their high neutron absorption cross sections.[7] Furthermore, lanthanides can form segregated phases in nuclear fuels, rather than homogeneous solid solutions with actinides, leading to hot spots and structural instability under reactor conditions.[8] This challenge originates from the comparable ionic radii, oxidation states, and coordination geometries of trivalent actinides and lanthanides.[9,10]

Despite this similarity, a fundamental distinction exists in their bonding nature. Actinides exhibit a higher degree of covalency in metal–ligand bonding, particularly with soft donor atoms such as nitrogen and sulphur, whereas lanthanide bonding remains ionic.[11] This subtle difference in bonding behaviour has been exploited in designing selective extractants that utilise soft donor atoms to bind actinides over lanthanides preferentially. As a result, several nitrogen-donor extractants, including bis-triazinylpyridine (BTP) and its derivatives, have been developed for selective actinide partitioning within advanced separation strategies such as the SANEX (selective actinide extraction) process.[12]

While early alkylated BTP ligands demonstrated promising Am/Eu selectivity, their practical utility was limited by poor acid stability, high aqueous solubility, and vulnerability to radiolytic degradation, especially due to the presence of oxidisable benzylic C–H bonds.[13] To overcome these issues, several modified structures were introduced. Annulated-ring analogues such as bis-annulated triazinylpyridines (BATPs) displayed

---

[a] *Homi Bhabha National Institute, Anushakti Nagar, Mumbai, Maharashtra 400 094, India. E-mail: jselva@igcar.gov.in*

[b] *Integrated Nuclear Recycle Plant, Nuclear Recycle Board, Bhabha Atomic Research Centre, Kalpakkam, Tamil Nadu 603 102, India*

improved radiolytic and hydrolytic stability.[14] Likewise, tetradentate ligands like CyMe$_4$BTBP and CyMe$_4$BTPhen enhanced actinide extraction performance, though with drawbacks like slow extraction kinetics, lanthanide co-extraction, and difficulty in actinide stripping.[15,16] Non-heterocyclic N-donor ligands, such as nitrilotriacetamide (NTAamide), were also explored for actinide separation at low acidity but exhibited relatively poor separation factors.[17] Similarly, attempts to reduce ligand basicity by replacing the pyridine core with less basic moieties like pyrazine showed limited improvement in selectivity.[18]

A notable advancement was made by Trumm *et al.* (2011), who introduced camphor substituents at the 5- and 6-positions of the triazine rings in BTP, yielding a novel ligand: bis-2,6-(5,6,7,8-tetrahydro-5,9,9-trimethyl-5,8-methano-1,2,4-benzotriazin-3-yl)pyridine (CA-BTP).[19] This camphorquinone-derived extractant offered several advantages over earlier analogues, including: high Am/Eu separation factors (~100), better solubility in 1-octanol (an alcohol-based diluent), superior acid and radiolytic stability, faster extraction kinetics and easier back-extraction of Am(III).

Despite its promising attributes, CA-BTP has remained underutilised in solvent extraction flowsheets, mainly due to limitations in large-scale synthesis, reproducibility of high-purity batches, and the complexity of purification.[20] However, its potential has been explored in solid-phase systems, where CA-BTP was immobilised on silica or polymer supports and combined with co-extractants like TEHDGA. These studies demonstrated good selectivity and complete actinide stripping under mild acidic conditions, without chelating agents like EDTA, offering practical advantages for large-scale operations.[21–24] While prior studies have focused on extraction performance, detailed investigations into the physicochemical behaviour of CA-BTP—such as acid uptake, interfacial behaviour, nitrate dependency, thermodynamic parameters, and extraction stoichiometry—have not been thoroughly reported. Comparative performance in different diluents, particularly alcohols like iso-decanol (IDA), remains unexplored. IDA offers unique advantages such as a high boiling point, low aqueous solubility, and improved phase separation, making it a promising alternative to conventional diluents.

In this study, we report the scalable synthesis and comprehensive evaluation of CA-BTP for the selective separation of ^{241}Am and ^{244}Cm(III) from acidic HLW. The ligand was synthesised from low-cost precursors (pyridine-2,6-dicarboxylic acid and camphorquinone) *via* a five-step route, with purification using gradient polarity silica gel chromatography. Structural confirmation and purity assessment were performed using FT-IR, UV-visible spectroscopy, ^{1}H NMR, ESI-MS, and TG–DSC.

The extraction efficiency, selectivity, and phase behaviour of CA-BTP were examined in two alcohol-based diluents: 1-octanol and IDA. Parameters including acid uptake, nitrate ion concentration, temperature, interfacial tension, and metal loading were systematically studied to understand the extraction mechanism and determine key thermodynamic quantities (ΔH, ΔG, ΔS). Slope analysis was conducted to estimate metal–ligand complex stoichiometry, while back-extraction performance was evaluated using mild aqueous nitric acid without synergists or complexants.

The findings offer new mechanistic insight into CA-BTP's extraction behaviour and establish its potential for application in advanced solvent extraction flowsheets for minor actinide partitioning under acidic HLW conditions.

2. Materials, synthesis procedure and methods

2.1. Materials

All chemicals and solvents were procured from commercial suppliers and used as received unless stated otherwise. Pyridine-2,6-dicarboxylic acid (PDCA) and camphorquinone (CQ) were obtained from Central Drug House (CDH), India. Anhydrous organic solvents such as methanol, ethanol, dimethylformamide (DMF), and dichloromethane (DCM), as well as reagents including phosphorus oxychloride (POCl$_3$), hydrazine monohydrate, and 25% aqueous ammonia, were supplied by Sisco Research Laboratories (SRL), India. Isodecanol (IDA) and 1-octanol were used as organic diluents. All aqueous solutions were prepared using Type-I water (resistivity ≥ 18 MΩ cm). Volumetric glassware was oven-dried before use.

Simulated high-level waste (SHLW) was prepared using nitrate salts of Y, La, Ce, Eu, Nd, Sm, Rh, Ru, and Pd. Active extraction studies were conducted using ^{241}Am and ^{154}Eu radiotracers obtained from actual HLW. A minor actinide–lanthanide-rich feed solution was generated by pre-extraction using 0.2 M tetra-ethyl-hexyl diglycolamide (TEHDGA) in 15% IDA-*n*-dodecane.

2.2. Synthesis of CA-BTP

The target ligand, bis-2,6-(5,6,7,8-tetrahydro-5,9,9-trimethyl-5,8-methano-1,2,4-benzotriazin-3-yl)pyridine (CA-BTP), was synthesised in five steps starting from PDCA and camphorquinone. In the first step (Scheme 1), dimethyl pyridine-2,6-dicarboxylate (PDC) was prepared by refluxing PDCA (0.3 mol) in methanol with concentrated sulfuric acid as a catalyst. The reaction was carried out for 12 hours in the presence of molecular sieves, followed by crystallisation and vacuum drying. The yield was 89%, and the product was confirmed by FT-IR spectroscopy, showing characteristic carbonyl and pyridine bands.

In the second step (Scheme 2), PDC (0.03 mol) was reacted with 25% aqueous ammonia (80 mL) at 313 K for 12 hours to yield pyridine-2,6-dicarboxamide (PDA), which crystallised upon cooling. The purified product exhibited a melting point of 605 K and FT-IR peaks consistent with amide and pyridine functionalities. The third step involved conversion of PDA to

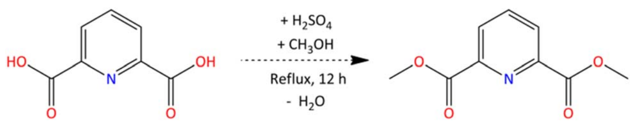

Scheme 1 Dimethyl-pyridine-2,6-dicarboxylate (PDC) from pyridine-2,6-dicarboxylic acid (PDAC).

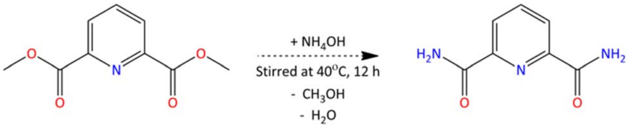

Scheme 2 Pyridine-2,6-dicarboxamide (PDA) from dimethyl pyridine-2,6-dicarboxylate (PDC).

Scheme 3 Pyridine-2,6-dicarbonitrile (PDN) from pyridine-2,6-dicarboxamide (PDA).

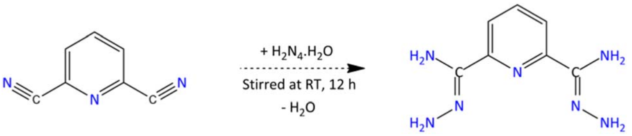

Scheme 4 Pyridine-2,6-dicarbohydrazonamide (PDH) from pyridine-2,6-dicarbonitrile (PDN).

pyridine-2,6-dicarbonitrile (PDN) using phosphorus oxychloride in chilled DMF (Scheme 3), followed by heating and hydrolysis. The isolated product displayed strong IR absorption for nitrile and aromatic nitrogen groups, yielding 75%.

In the fourth step (Scheme 4), PDN (0.04 mol) was converted to pyridine-2,6-dicarbohydrazonamide (PDH) by reaction with 75% hydrazine hydrate at ambient temperature. The product was filtered, washed with ethanol, recrystallised from water, and dried under vacuum. Finally, in the fifth step (Scheme 5), PDH was condensed with camphorquinone (0.05 mol) in ethanol at 120 °C for 30 hours in the presence of molecular sieves. Reaction progress was monitored using UV-visible spectroscopy and thin-layer chromatography (TLC). A caramel-coloured solid was obtained in 82% yield. The final crude product was purified by gradient polarity silica gel column chromatography using ethyl acetate/petroleum ether mixtures.

The purification process involved careful elution from 20% to 100% ethyl acetate in petroleum ether, allowing effective separation of unreacted starting materials and by-products. Each fraction was characterised by Fourier-transform infrared spectroscopy (FT-IR: Thermo Scientific Nicolet iS5 with iD1 transmission accessory operated *via* OMNIC 9.8.372 software), proton nuclear magnetic resonance (^{1}H NMR, AVANCE III 500 MHz), and electrospray ionisation mass spectrometry (ESI-MS). Thermal stability and decomposition behaviour were assessed using thermogravimetric-differential scanning calorimetry (TG-DSC) on a Netzsch STA 449 F5 instrument, with a heating rate of 10 K min^{-1} under nitrogen.

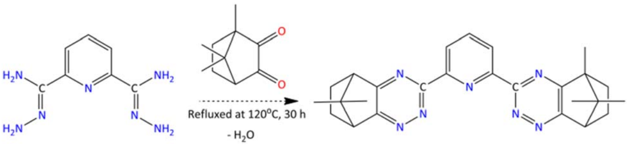

Scheme 5 Synthesis of camphor-bis-triazinyl pyridine (CA-BTP).

2.3. Monitoring, purification, and characterisation of CA-BTP with distribution and thermodynamic studies

Ultraviolet-visible (UV-vis) spectroscopy was employed to monitor the progress of the final reaction step (Scheme 5) and to study acid-dependent electronic transitions. Spectra were recorded between 200 nm and 500 nm in quartz cuvettes using a Hitachi UH5300 spectrophotometer. Aliquots were withdrawn regularly during the reaction, evaporated, redissolved in ethanol, and scanned at ambient temperature. Gradient-purified fractions were analysed for solubility and phase behaviour in 1-octanol and IDA. Their extraction efficiency was screened using tracer-level ^{241}Am and ^{154}Eu in 1 M HNO_3, and the best-performing fractions were selected for further studies.

Solvent extraction experiments were conducted under ambient conditions (298 ± 2 K) using equal volumes of organic and aqueous phases (O/A = 1 : 1), and the mixtures were shaken for 60 minutes to ensure equilibrium. Organic phases were prepared by dissolving CA-BTP in either 1-octanol or IDA at required concentrations (typically 0.05–0.1 M). After phase separation, distribution ratios (D) were calculated based on metal ion concentrations in each phase, as measured by α-spectrometry (Canberra Alpha Analyst operated with Genie 2000 software version 3.4.1) and γ-spectrometry (Baltic Scientific Co-axial P-type high-purity germanium (HPGe) detector with an energy resolution of 1.3 keV (FWHM) at 122 keV) or Inductively Coupled Plasma Optical Emission Spectroscopy (ICP-OES, Horiba Jobin Yvon Ultima 2), depending on the experiment. The organic phases were also examined for phase clarity and stability under various acid concentrations.

Acid uptake experiments were performed by equilibrating CA-BTP solutions in alcohol-based diluents with HNO_3 of varying concentration (0.1–4.0 M). After phase separation, acid content in both phases was quantified by titration using standardised NaOH solution with phenolphthalein as an indicator. Additional validation was performed using an automated titrator (Mettler Toledo DGi111-SC) with pre-neutralised ethanol for organic phase titration.

Interfacial tension (IFT) measurements were carried out using the platinum rod method to assess diluent compatibility, phase disengagement, and surface activity of CA-BTP under neutral and acidic conditions. Thermodynamic studies were performed by conducting extractions at various temperatures (298–333 K) using thermostated water baths. Distribution ratios at each temperature were used to derive apparent thermodynamic parameters (ΔH, ΔG, ΔS) *via* Van't Hoff analysis.

Mechanistic investigations included slope analysis by varying CA-BTP concentration (log D *vs.* log[CA-BTP]) under constant nitrate and acidity, enabling the determination of metal-to-ligand stoichiometry. Nitrate dependence was also studied by varying $NaNO_3$ concentration at fixed HNO_3, to examine its role in complex formation and phase stability. Finally, back-extraction (stripping) behaviour was evaluated by contacting the metal-loaded organic phases with 0.01 M HNO_3 under mild conditions, assessing the reversibility of the extraction process.

3. Results and discussion

The synthesis pathway from dimethyl pyridine-2,6-dicarboxylate (PDC) to pyridine-2,6-dicarbohydrazonamide (PDH) demonstrates notable variations in melting temperature of the intermediates. The initial ester compound (PDC) exhibits a melting point of 396 K, which significantly increases to 605 K upon conversion to the amide derivative (PDA), indicating enhanced thermal stability due to strong intermolecular hydrogen bonding. Subsequent transformation to the nitrile (PDN) lowers the melting point to 402 K, reflecting reduced hydrogen bonding capacity. Finally, the introduction of hydrazone functionality in PDH elevates the melting point again to 513 K, consistent with increased molecular interactions and structural rigidity.

Further, the progression of the synthesis from PDCA to PDH (Scheme 1–4) was confirmed through characteristic FT-IR spectral features observed at each step. In Step 1, the formation of dimethyl pyridine-2,6-dicarboxylate (PDC) was indicated by strong absorption bands at 1742 cm^{-1} (C=O stretching of ester), 1571 cm^{-1} (C=N of the pyridine ring), and 1244 cm^{-1} (C–O of ester). In Step 2, conversion to pyridine-2,6-dicarboxamide (PDA) was evident from broad N–H stretching bands between 3402–3226 cm^{-1}, an amide C=O band at 1678 cm^{-1}, and a retained C=N stretch at 1588 cm^{-1}, along with N–H bending at 1438 cm^{-1}. The successful transformation to pyridine-2,6-dicarbonitrile (PDN) in Step 3 was confirmed by a sharp C≡N stretching band at 2250 cm^{-1}, along with C=N and C=C absorptions at 1574 and 1442 cm^{-1}, respectively. Finally, in Step 4, the formation of pyridine-2,6-dicarbohydrazonamide (PDH) was characterized by broad N–H stretching vibrations in the 3448–3245 cm^{-1} range, consistent with the introduction of hydrazonamide groups. Fig. 1Sa depicts the FT-IR spectra of each step products obtain among various synthetic batches (Fig. 1Sb), which confirms the reproducibility of the synthesis and product purity.

3.1. Monitoring CA-BTP reaction progress by UV-visible spectroscopy

The progress of the condensation reaction between camphorquinone (CQ) and pyridine-2,6-dicarbohydrazonamide (PDH) was systematically monitored using UV-visible spectroscopy, enabling real-time assessment of electronic transitions associated with the reactants and intermediates. Spectra were recorded in ethanol at room temperature over the 200–500 nm range at selected time intervals during the reaction.

The spectrum of pure camphorquinone exhibited a characteristic intense band at 460 nm, attributed to an n → π* transition involving the diketone chromophore (Fig. 1). This band, corresponding to the excitation of non-bonding electrons on the carbonyl oxygen atoms, accounts for the deep yellow colouration of CQ in solution. In contrast, PDH displayed two distinct absorption features: a sharp π → π* transition at 212 nm due to the aromatic pyridine ring, and an n → π* transition at 303 nm arising from lone pair electrons on the hydrazonamide nitrogen atoms.[25,26]

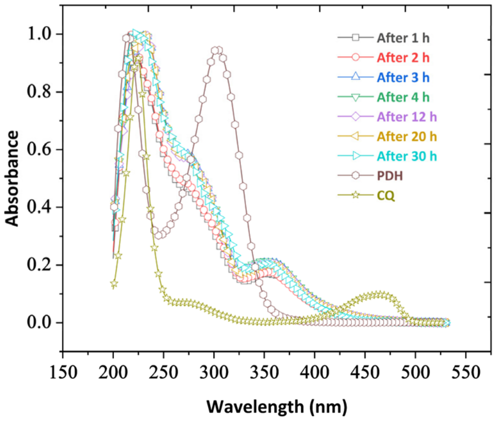

Fig. 1 UV-visible spectra of the individual reactants and the reaction mixture recorded at different time intervals.

Upon mixing CQ and PDH in ethanol under reflux, the spectrum of the reaction mixture showed the gradual disappearance of the 460 nm CQ band, confirming its consumption as the condensation proceeded. Concurrently, new absorption bands emerged in the 220–400 nm range, which intensified over time. These bands are associated with π → π* transitions within extended conjugated systems or nascent triazine-containing intermediates. The progressive increase in absorbance at 275 nm and 350 nm during the first four hours suggested rapid formation of intermediate species, followed by a gradual levelling-off of intensity, indicating completion of the reaction around the 24–30 hours mark.[27]

Notably, the complete disappearance of the 460 nm CQ peak by 24 hours confirmed its exhaustive participation in the reaction, while the development of new features in the UV region pointed to the formation of the final CA-BTP structure. These spectral changes are consistent with reported behaviour for BTP-type ligands, where triazine ring formation leads to characteristic π → π* transitions in the 250–350 nm region.[28] indicating possible formation of extended conjugated systems or intermediates.

Thus, UV-vis spectroscopy proved a valuable tool for non-invasively tracking the condensation process, validating both reactant consumption and the formation of conjugated triazine–pyridine structures central to CA-BTP.

3.2. Characterisation of CA-BTP fractions from gradient elution chromatography

Following the multistep synthesis of the target ligand, bis-2,6-(5,6,7,8-tetrahydro-5,9,9-trimethyl-5,8-methano-1,2,4-benzotriazin-3-yl)pyridine (CA-BTP), the crude product was subjected to gradient polarity silica gel column chromatography using ethyl acetate and petroleum ether as the mobile phase.

The column fractions were collected sequentially and analysed using multiple spectroscopic and thermal techniques to identify the chemically pure ligand fraction and understand the evolution of structural features during purification. Among the fractions collected, fractions eluted with 80% and 100% ethyl acetate were determined to possess the most consistent and diagnostic spectral attributes corresponding to the fully formed CA-BTP ligand, free from unreacted precursors or condensation intermediates. The fractions were subjected to detailed FT-IR, ^{1}H NMR, ESI–MS, and TG-DSC analyses, the results of which are discussed below.

3.2.1. Functional group analysis by FT-IR. The stepwise formation and purification of the CA-BTP ligand were systematically tracked using FT-IR spectroscopy across column fractions eluted with increasing polarity (20% to 100% ethyl acetate in petroleum ether), as shown in Fig. S2. The spectrum of camphorquinone, used as the reference precursor, exhibited a sharp and intense C═O stretching band at 1748 cm^{-1}, attributed to its conjugated diketone functionality. This band served as a diagnostic feature for monitoring the disappearance of unreacted ketone during condensation. In the early fractions eluted with low polarity solvents (20–30%), this carbonyl band persisted strongly, indicating significant carryover of unreacted or partially condensed camphorquinone. These fractions also showed poorly resolved aromatic C═N stretches in the 1580–1600 cm^{-1} region.[29]

With increasing elution strength, particularly in the 50–80% ethyl acetate fractions, the C═O band at 1728 cm^{-1} progressively weakened and eventually disappeared, indicating complete consumption of the carbonyl precursor. Simultaneously, new spectral features became prominent: a strong C═N stretching band appeared at 1585–1590 cm^{-1}, characteristic of the pyridine and triazine aromatic cores; a distinct ring-breathing vibration of the 1,2,4-triazine appeared at 1345–1350 cm^{-1}; and a medium-intensity C–N stretching band emerged at ∼1270 cm^{-1}. Moderately broad N–H stretching vibrations near 3230 cm^{-1} in these later fractions further supported the formation of N–NH–C linkages connecting the triazine and pyridine subunits. In the final, most polar fraction (100% ethyl acetate), the spectrum showed clean and sharp features consistent with the fully condensed ligand, including complete disappearance of the C═O vibration and well-resolved triazine and aromatic bands, indicating that this fraction (as well as Fraction 7, corresponding to 80%) contained chemically pure CA-BTP. The spectral evolution across the gradient confirms the effective chromatographic resolution of unreacted precursors from the fully formed ligand and supports the structural assignment of the purified product.[30]

3.2.2. Mass spectral and NMR (^{1}H) analysis. Fig. S3a–c depicts the mass spectra of fractions collected with the eluent composition of 20% EA/PE, 80% EA/PE, and 100% EA. The mass spectrometric data for the 20% EA/PE product indicate the presence of unreacted camphorquinone as the major component. The molecular ion peak at *m*/*z* 166 corresponds to [M]$^+$, confirming the presence of the parent molecule. Fragmentation patterns support this assignment: the peak at *m*/*z* 138 results from ring cleavage with loss of a CO group [M–CO]$^+$, and *m*/*z* 136 corresponds to the further loss of a hydrogen molecule [M–CO–H$_2$] $^+$. Additional peaks at *m*/*z* 158 and *m*/*z* 174 are due to C–C bond cleavages, indicating loss of a methyl group and subsequent protonation, respectively. A peak at *m*/*z* 212 suggests C–C cleavage followed by ethyl ester formation, indicating minor transformation products. The ^{1}H NMR spectrum, Fig. S4a, supports this interpretation, showing multiple singlets in the 0.95–1.11 ppm range for methyl groups, and complex multiplets from 1.59 to 2.64 ppm, consistent with the camphor skeleton. Very low-intensity extra peaks at 0.90, 1.002, 1.47–2.97 ppm suggest the presence of camphorquinone-derived by-products, potentially formed during side reactions. Overall, both MS and NMR data suggest that this fraction primarily contains unreacted camphorquinone with minor amounts of transformation products and by-products.

The mass spectrometry data for the 80% EA/PE fraction show prominent peaks at *m*/*z* 454 and *m*/*z* 476, corresponding to the protonated molecule [M–H]$^+$ and sodium adduct [M–Na]$^+$, respectively. These peaks indicate a molecular weight of 453 g mol^{-1}, suggesting the formation of CA-BTP from the camphorquinone and pyridine-2,6-dicarbohydrazonamide (PDH). The ^{1}H NMR spectrum (Fig. S4b), further supports this conclusion, with singlets at δ 0.679, 1.132, and 1.50 ppm, each integrating to 6 protons, consistent with multiple gem-dimethyl groups or symmetrical structural motifs. Multiplets in the region of δ 2.04–2.12 ppm and 2.31–2.37 ppm suggest the presence of methylene groups adjacent to electron-withdrawing groups like carbonyls or aromatic rings. A doublet at δ 3.30 ppm (2H) likely corresponds to methylene protons adjacent to an electronegative atom or unsaturated centre. The downfield signals at δ 8.10 (t, 1H) and δ 8.72–8.75 (m, 2H) are characteristic of aromatic or heteroaromatic protons, indicating the incorporation of an aromatic ring system in the product. The MS and NMR data confirm that this fraction primarily consists of a major reaction product resulting from extensive structural modification of the starting material, with minimal unreacted camphorquinone present.

The mass spectrometry data for the 100% EA fraction display similar to 80% EA/PE fraction. A peak at *m*/*z* 437 is also observed, which can be attributed to the loss of a methane unit [M–CH$_4$–H]$^+$, indicating minor fragmentation or rearrangement. Peaks at *m*/*z* 481 and *m*/*z* 598 likely represent adducts or aggregation with fragmented species, which are sometimes observed in highly purified or concentrated samples. The ^{1}H NMR spectrum (Fig. S4c), is essentially the same as that of the 80% fraction, showing singlets at δ 0.679, 1.132, and 1.50 ppm, each integrating to 6H, suggesting multiple methyl groups in symmetrical environments. The multiplet at δ 2.04–2.12 ppm (6H) and δ 2.31–2.37 ppm (2H) indicates methylene groups near functional groups like carbonyls or aromatic rings. The signal at δ 3.30 ppm (d, 2H) is again consistent with protons adjacent to a de-shielding group. Downfield signals at δ 8.10 ppm (t, 1H) and δ 8.72–8.75 ppm (m, 2H) are indicative of aromatic or heterocyclic proton environments. A small multiplet around δ 2.5 ppm may indicate minor structural variations, such as incomplete ring closure or a small proportion of side products. The mass and NMR spectra confirm that the 100% EA fraction contains a purified form of the major reaction product, with minimal/no contamination or unreacted starting material.

3.2.2.1. Thermal (TG-DSC) analysis. Thermogravimetric (TG) and differential scanning calorimetry (DSC) analyses were performed to evaluate the thermal stability, decomposition characteristics, and physical phase behaviour of the eluted fractions from gradient chromatography, in comparison to pure camphorquinone (CQ), as presented in Fig. 2a and b. The TG trace for unreacted camphorquinone, along with that of the 20% EA/PE eluted fraction, revealed a nearly complete mass loss of ∼100% and ∼97%, respectively, indicating that these samples primarily comprise low-molecular-weight, volatile organic species. This high volatility is consistent with the known sublimation behaviour of camphorquinone and corroborates the presence of unreacted precursor in the early eluted fractions. The DSC trace of camphorquinone exhibited an initial endothermic transition at ∼344 K without significant mass loss, which can be assigned to a solid–solid phase transition, possibly linked to a crystalline rearrangement or polymorphic transformation. This was followed by sharp endothermic peaks concurrent with rapid and complete mass loss, consistent with melting followed by sublimation, typical for small, rigid, bicyclic ketones that do not form a stable melt phase but instead vaporise upon heating.

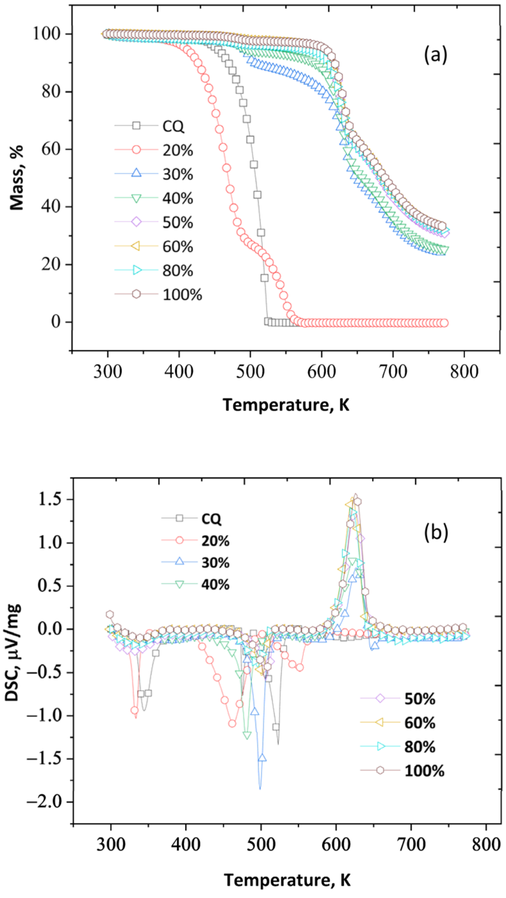

Fig. 2 (a) TG and (b) DSC traces of camphorquinone and column fractions obtained with gradient polarity.

In contrast, the thermal profiles of fractions eluted with higher ethyl acetate content (50–100%) displayed substantially altered behaviour, indicating progressive enrichment of a new, more stable product. These more polar fractions exhibited two minor endothermic events in 352–362 K and 475–505 K, each associated with a modest mass loss of ∼5%. The first event may be attributed to the release of residual solvent or loosely bound moisture, while the second is likely due to the loss of minor thermolabile by-products or residual condensation intermediates. Notably, a broad and intense exothermic peak centred between 619 K and 625 K was consistently observed in the DSC profiles of these purified fractions. This thermal event is accompanied by a substantial mass loss of ∼75% and is characteristic of the decomposition of the heterocyclic BTP framework, likely involving cleavage of the triazine and pyridine rings, and the release of nitrogen-rich gaseous by-products. Such behaviour aligns with reported thermal decomposition mechanisms of structurally related aromatic triazines and other nitrogen-rich heterocycles, where decomposition initiates *via* ring scission and radical recombination processes at elevated temperatures.[31]

No sharp melting point was observed for the purified fractions within the typical 353–373 K range. Instead, the samples exhibited a slow and progressive darkening from yellow to reddish-brown prior to decomposition, suggesting a phase transformation involving rearrangement or molecular fragmentation, rather than classical melting. This behaviour—transitioning directly from solid to decomposition—is frequently observed in rigid, bicyclic and conjugated frameworks where extensive π-delocalization and intermolecular interactions suppress true melting. The absence of a liquid phase formation supports the notion that the purified CA-BTP is thermally metastable and undergoes direct breakdown upon heating, consistent with its robust solid-state structure.[32]

Overall, the thermal analysis unequivocally distinguishes early fractions, which are dominated by low-stability, volatile precursors, from later fractions enriched in thermally resilient CA-BTP. The purified ligand displays excellent thermal resistance up to ∼573 K, reinforcing its suitability for solvent extraction processes involving elevated temperatures or extended contact times. Moreover, its predictable decomposition profile supports the feasibility of post-use thermal treatment strategies, making it a promising candidate for integration into sustainable separation flowsheets for actinide partitioning.

3.3. Assessment of efficiency and selectivity in metal ion uptake

The extraction performance of chromatographically separated CA-BTP fractions was evaluated through detailed radiotracer experiments using ^{241}Am (2.70 mCi L^{-1}) and ^{154}Eu(III) (0.94 mCi L^{-1}) in 1.0 M HNO_3—a representative acidity chosen to mimic the conditions of actual high-level radioactive liquid waste (HLW) encountered in advanced partitioning flowsheets. The solvent system employed consisted of 0.1 M CA-BTP (gradient-eluted fractions) in 1-octanol. Under these conditions, the relative uptake of actinides and lanthanides directly measures the ligand's functional purity and selectivity.

Fractions eluted with low polarity eluents (20–30% ethyl acetate in petroleum ether) exhibited negligible extraction of both ^{241}Am and ^{154}Eu(III), confirming that these early fractions primarily contain unreacted camphorquinone or incompletely condensed intermediates, as supported by FT-IR and mass spectral data. These species lack the required N-donor coordination architecture for selective actinide complexation and contribute little to overall extraction.

From the 40% EA/PE fraction onward, a marked increase in Am(III) uptake was observed, with distribution ratios rising sharply. Maximum uptake efficiency was recorded for the 100% EA fraction, which achieved 87.6% extraction of ^{241}Am(III) under standard conditions (Fig. 3a). In contrast, ^{154}Eu(III) remained almost entirely unextracted across all fractions, including those with high ^{241}Am(III) affinity. The resulting separation factor ($SF_{Am/Eu}$) exceeded 150–280 for the purified fractions, establishing a highly selective actinide–lanthanide separation profile. This pronounced selectivity likely arises from the CA-BTP ligand's tridentate soft nitrogen donor environment, which preferentially stabilises the more polarisable 5f orbitals of actinides over the 4f orbitals of lanthanides—an effect supported by covalency-driven bonding trends reported for other BTP-type ligands.

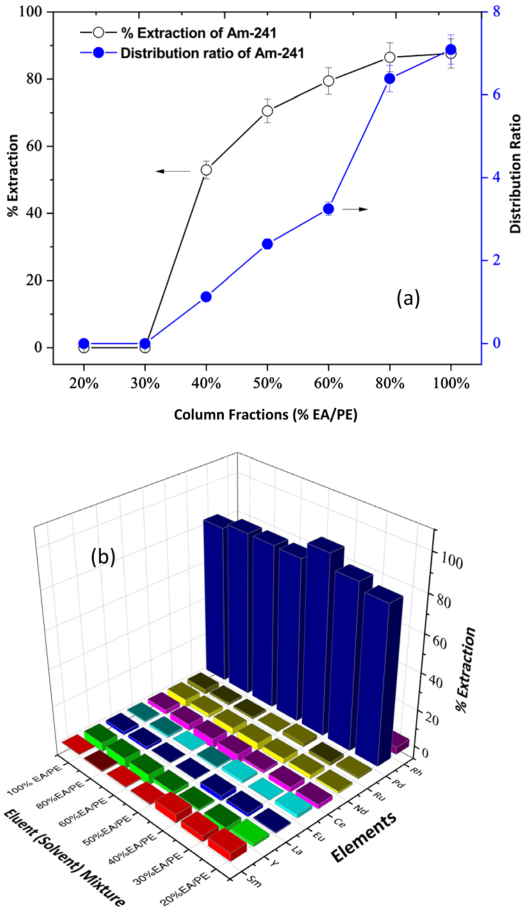

Fig. 3 (a) Distribution ratio and % extraction of Am-241 for various column fractions; (b) selectivity: % extraction of lanthanides and noble metals from simulated high-level liquid waste (SHLW) at 1.0 M HNO_3 feed acidity.

To assess the ligand's behaviour in more complex environments, extraction studies were further extended to simulated high-level liquid waste (SHLW) containing a wide range of competing elements, including rare earths and noble metals (Table S1). The purified CA-BTP fractions (80–100% EA/PE) demonstrated robust selectivity even under this multicomponent matrix. Negligible extraction was observed for lanthanides such as Sm(III), La(III), Nd(III), Ce(III), Y(III), and Eu(III), and for noble metals like Ru and Rh (Fig. 3b). Notably, Pd(II) exhibited high co-extraction (∼86%) across all fractions containing active CA-BTP. This unexpected affinity for Pd(II) may reflect favourable interactions between Pd(II) and the ligand's electron-rich nitrogen and amide donor environments, suggesting square-planar complexation or ligand-induced stabilisation of soft metal centres. While this Pd(II) extraction may present challenges for selective Am(III) recovery in mixed-waste scenarios, it may also offer a potential route for dual Pd/Am(III) separation—a feature warranting further mechanistic investigation.

The extraction profile as a function of chromatographic fractionation thus demonstrates a strong correlation between chemical purity and metal ion uptake efficiency. Only the later fractions—confirmed by IR, NMR, and MS to be structurally pure CA-BTP—exhibited efficient and selective ^{241}Am(III) uptake. In contrast, fractions containing residual precursor or incomplete condensation products showed diminished or negligible performance. Moreover, the purified ligand exhibited excellent solubility and acid tolerance in 1-octanol, with no third-phase formation even under high acidity. These physicochemical features suggest practical feasibility for use in partitioning flowsheets.

The extraction data affirm that the 80–100% EA/PE window defines the optimal purification range for obtaining functionally active CA-BTP. The combined high selectivity, low co-extraction of matrix species, and compatibility with alcohol-based diluents support the potential deployment of this ligand in simplified, DGA-free solvent extraction systems for minor actinide separation. Accordingly, fractions from this elution range were pooled and used for all subsequent mechanistic, thermodynamic, and process-oriented investigations.

3.4. Solubility, acid stability and interfacial properties

An extractant's solubility and phase compatibility critically determine its utility in solvent extraction flowsheets, particularly under the demanding conditions encountered in high-level radioactive waste (HLW) treatment. The gradient-purified CA-BTP fractions exhibited distinct and composition-dependent solubility behaviour when evaluated in alcohol-based diluents, specifically 1-octanol and iso-decanol (IDA), known for their high polarity, chemical inertness, and process compatibility. Fractions eluted with 60–100% ethyl acetate in petroleum ether (EA/PE) produced clear, homogeneous solutions when redissolved in 1-octanol at concentrations up to 0.1 M, indicating successful removal of insoluble by-products and unreacted precursors (Fig. S5a). These purified fractions showed no signs of turbidity, emulsification, or precipitation even upon prolonged standing, supporting their selection for further extraction experiments.

The solubility profile of CA-BTP was also investigated in binary systems comprising varying ratios of IDA and *n*-dodecane. High solubility was retained in 80–100% IDA blends, forming homogeneous 0.1 M solutions with minimal agitation. However, significant interfacial precipitation was observed in the intermediate IDA blends (50–80%) upon contact with 1.0 M HNO_3 (Fig. S5b). This suggests reduced ligand solvation or possible self-aggregation in the presence of acid in these less polar systems. In contrast, neat 1-octanol and IDA maintained excellent phase integrity and stability even at 2.0 M HNO_3, highlighting their superior compatibility with the ligand. The better solvation performance of alcohol-rich diluents may be attributed to their protic nature and ability to form hydrogen bonds with the amide and pyridyl nitrogen atoms of CA-BTP, facilitating efficient solvation and suppressing aggregation.

Given the requirement to maintain ligand integrity under nitric acid contact (typically 0.5–2.0 M in HLW applications), the acid-phase stability of CA-BTP was also examined. Upon equilibration with 1.0 M HNO_3, purified CA-BTP fractions in 1-octanol (particularly from ≥50% EA/PE) exhibited no visible precipitation or third-phase formation over 1 and 24 hours. A gradual colour changes from yellow to reddish-brown was observed (Figs. S4c and d), which was attributed to the protonation of triazine and pyridine nitrogen atoms, altering the ligand's electronic structure without compromising solubility. This colour shift, while indicating electronic rearrangement, did not interfere with metal extraction, as evidenced by consistent distribution ratios in parallel experiments.

UV-vis spectroscopy of CA-BTP in ethanol further substantiated this protonation behaviour. At neutral pH (7.1), the ligand displayed a dominant absorption at 275 and 295 nm, assigned to a $\pi \rightarrow \pi^*$ transition in the conjugated aromatic core. Acidification to pH 3.2 and below induced notable spectral changes: a bathochromic shift and a hyperchromic response were observed at 265 and 305 nm (Fig. 4), reflecting LUMO stabilisation due to protonation and enhanced delocalisation across the ligand framework. This indicates increased π-conjugation upon acid interaction, which may enhance the ligand's ability to participate in metal coordination under acidic extraction conditions. At stronger acidities (0.5 M H^+ and above), further nonlinear spectral responses were recorded, suggesting alterations in solute–solvent and ligand–acid interactions, likely influencing both electronic configuration and extraction kinetics.

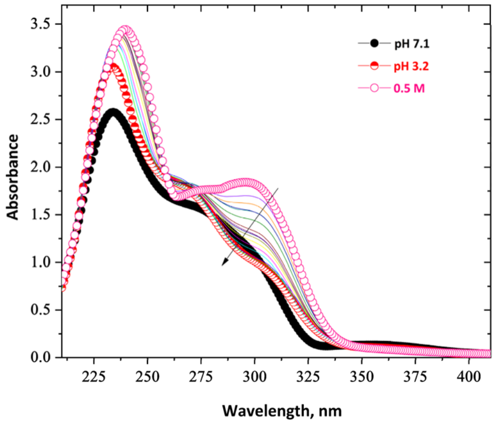

Fig. 4 UV-visible spectra of CA-BTP in ethanol at pH 7.1, pH 3.2, and under acidic conditions (0.5 M H^+); time-dependent spectral changes were also monitored under 0.5 M H^+ acidity.

In addition to chemical compatibility, the phase separation characteristics of CA-BTP solutions were evaluated through interfacial tension (IFT) measurements using the platinum rod method. Pure IDA exhibited a native surface tension of 27.69 mN m^{-1}, slightly lower than 1-octanol (27.72 mN m^{-1}). Upon equilibration with an aqueous mixture of 0.5 M HNO_3 and 0.5 M $NaNO_3$, both diluents demonstrated reduced interfacial tension, with CA-BTP-loaded 1-octanol showing marginally lower IFT than the corresponding IDA solution. Interestingly, although IDA-based systems had higher interfacial tension values (typically favouring faster disengagement), they displayed slower phase separation, requiring 10–15 minutes to form a sharp interface. In contrast, CA-BTP in 1-octanol achieved phase disengagement within seconds, despite its viscosity and interfacial tension. This apparent contradiction likely arises from the higher viscosity of IDA and possible interfacial frothing or microemulsion formation than CA-BTP/1-octanol, as visually confirmed during experiments.

Further examination revealed that CA-BTP behaves as a surface-inactive species under neutral conditions in both diluents (Table S2). However, upon exposure to acidic aqueous phases (*e.g.*, HNO_3–$NaNO_3$ mixtures), the ligand exhibited enhanced interfacial activity, evidenced by significant reductions in IFT. This observation is consistent with prior studies on protonated BTP derivatives, where protonation increases amphiphilicity, enhances surface activity, and facilitates accelerated metal ion transport across the aqueous–organic interface. Such behaviour is favourable in biphasic systems where rapid extraction kinetics and clear phase boundaries are desired.

While extraction efficiency was broadly comparable between IDA and 1-octanol, IDA offered marginally higher distribution ratios for ^{241}Am(III) and ^{244}Cm(III), likely due to improved solubility and clearer organic phases. Nonetheless, 1-octanol demonstrated superior operational characteristics overall—including acid compatibility, rapid phase disengagement, and stable extraction profiles—without needing co-diluents or phase modifiers. Additional experiments were conducted to further investigate extraction behaviour and underlying mechanisms using both 1-octanol and IDA.

Together, these results establish CA-BTP as a highly soluble, acid-tolerant, and interfacially stable ligand in alcohol-based diluents. Its compatibility with nitric acid media and its robust phase behaviour support its application in advanced solvent extraction flowsheets, particularly those targeting minor actinide partitioning from complex HLW matrices.

3.5. Acid uptake behaviour of pure and CA-BTP-containing diluents

The extraction of nitric acid into the organic phase is a critical determinant of extractant performance in solvent systems designed for minor actinide partitioning. Acid uptake directly influences ligand availability, metal ion selectivity, and overall phase stability. In particular, the extent of protonation of nitrogen-donor ligands such as bis-triazinylpyridines (BTPs) plays a central role in modulating their coordination behaviour.[33] To evaluate the acid compatibility and uptake behaviour of CA-BTP, systematic titrimetric studies were conducted using both neat alcohol diluents—1-octanol and iso-decanol (IDA)—as well as their CA-BTP-loaded counterparts.

Initial acid uptake measurements were performed using pure diluents in the absence of ligand across a nitric acid concentration range of 0.1–2.0 M (Fig. 5). Both 1-octanol and IDA exhibited low but non-negligible acid uptake, consistent with their ability to form hydrogen-bonded HNO_3–alcohol adducts. At 1.0 M HNO_3, 1-octanol extracted 0.088 M of acid, compared to 0.072 M for IDA. The slightly lower uptake in IDA is attributed to its branched alkyl structure, which imposes steric constraints and reduces its capacity to engage in extended hydrogen bonding networks. These differences in acid affinity were quantified by calculating the basicity constant (K_H), yielding values of 0.015 for 1-octanol and 0.0098 for IDA.

The validity of this titrimetric approach was first verified using well-established extractant systems. The nitric acid uptake behaviour observed for 1-octanol and its mixtures with *n*-dodecane was compared with literature data reported by Geist *et al.*[34] Experimental data and computed results are shown in Fig. S6a–d. As shown in Fig. S6d, the acid uptake profile from the present study closely follows the trend reported by Geist, with a slope of 0.284 and an intercept of −0.1613 for the log $[H^+]_{org} - \log[E]_{org}$ *versus* $\log[H^+]_{aq}$ plot. Additionally, acid uptake data for 30% tributyl phosphate (TBP) and 0.2 M *tetra*(2-ethylhexyl)diglycolamide (TEHDGA) in *n*-dodecane yielded K_H values of 0.16 (slope = 1.44) and 1.73 (slope = 1.72), respectively, which are in close agreement with reported values (Fig. S5a and b), further confirming the method's reliability.[35,36] These experiments were conducted under controlled conditions using a calibrated auto titrator and were corrected for atmospheric CO_2 interference to ensure precision.

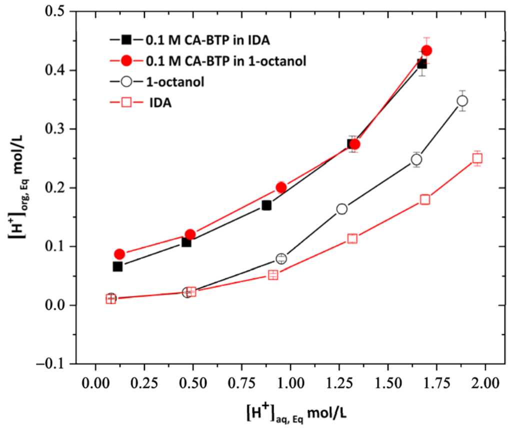

Fig. 5 Acid uptake by pure IDA, 1-octanol and 0.1 M CA-BTP/alcohol systems.

Following this, acid uptake experiments were carried out using 0.05 M CA-BTP solutions in 1-octanol and IDA. In each case, the presence of the ligand led to a measurable increase in acid extraction relative to the neat diluent. At 1.0 M HNO_3, the CA-BTP/1-octanol system extracted 0.20 M acid, while the CA-BTP/IDA system extracted 0.17 M, representing ∼12% and ∼9.8% enhancements, respectively. These increases reflect the direct participation of the CA-BTP ligand in acid binding, most likely through protonation of the electron-rich triazine and pyridyl nitrogen atoms.

Importantly, no precipitation or third-phase formation was observed in the CA-BTP/1-octanol system even at 2.0 M HNO_3. In contrast, the CA-BTP/IDA system exhibited visible precipitation within 1 hour under the same conditions, with solids accumulating at the organic–aqueous interface. This instability is attributed to the lower acid-buffering capacity of IDA and its reduced ability to solvate the protonated ligand. The data thus highlight the superior acid-phase compatibility of 1-octanol for CA-BTP-based systems.

To gain mechanistic insight, the acid–ligand interaction was modelled using the equilibrium:

$$E_{(org)} + n\mathrm{H}^+ + n\mathrm{NO_3}^- \rightleftharpoons E\cdot n\mathrm{HNO}_{3(org)}$$

Under the assumption of 1 : 1 HNO_3 dissociation and negligible nitrate competition, this simplifies to:

$$K_H = \frac{[E\cdot n\mathrm{HNO_3}]_{(org)}}{[E]_{(org)}[\mathrm{H}^+]_{aq}^{2n}}$$

Logarithmic transformation of the equilibrium expression for acid–ligand complexation facilitates linear fitting in the form:

$$\log\left(\frac{[E\cdot n\mathrm{HNO_3}]_{(org)}}{[E]_{(org)}}\right) = \log K_H + 2n\log[\mathrm{H}^+]_{aq}$$

A log–log transformation of this expression was applied to the acid uptake data for the CA-BTP/1-octanol system. The resulting plot of log D_{HNO_3} *versus* $\log[H^+]^2$ yielded a linear relationship with a slope consistent with $2n \approx 2$, indicating a proton-to-ligand stoichiometry of $n = 1$.[37] This result implies that CA-BTP primarily forms a monoprotonated complex under HLW-relevant acidity conditions.

The UV-vis spectral data (section 3.4) reflect electronic perturbations consistent with protonation of nitrogen donor sites and LUMO stabilisation, which are characteristic of monoprotonated aromatic systems (pH 3.2).

Altogether, the acid uptake behaviour of CA-BTP underscores the importance of diluent selection in extraction system design. While IDA offers lower intrinsic acid uptake, this comes at the cost of reduced proton buffering and greater risk of extractant precipitation. Conversely, 1-octanol balances moderate acid affinity, high ligand solubility, and excellent phase stability. These attributes justify the selection of both IDA and 1-octanol as suitable diluents for CA-BTP in downstream metal ion extraction and mechanistic studies. The apparent correlation between acid uptake capacity, protonation behaviour, and phase compatibility establishes a solid foundation for optimising the extraction performance of BTP-based ligands under challenging nuclear fuel cycle conditions.

3.6. Thermodynamic analysis: influence of temperature on trivalent actinide extraction by CA-BTP

To elucidate the thermodynamic characteristics governing metal–ligand interactions in CA-BTP-based extraction systems, the temperature dependence of ^{241}Am(III) and ^{244}Cm(III) extraction was systematically investigated in both 1-octanol and isodecanol (IDA) diluents. The extraction experiments were conducted using 0.05 M CA-BTP over a temperature range of 298–333 K, and the distribution ratios (D_{Am} and D_{Cm}) were measured at each temperature. As shown in Figs. S8a and S8b showed a clear inverse correlation between temperature and distribution ratio in both solvents, with D values decreasing steadily as temperature increased. This trend strongly indicates that the extraction of ^{241}Am(III) and ^{244}Cm(III) by CA-BTP is an exothermic process. This thermodynamic behaviour is consistent with previous studies on BTP-type extractants such as CyMe$_4$-BTP and OMe$_3$-BTP, where the metal complexation process is known to be enthalpy-driven and thus more favourable at lower temperatures.[38] The extraction is presumed to involve formation of neutral metal–ligand–nitrate complexes, which release energy upon formation in the organic phase.

To quantify the enthalpic contribution to extraction, the apparent enthalpy change (ΔH_{app}, kJ mol^{-1}) was calculated using the Van't Hoff equation:

$$\Delta H,\ \mathrm{kJ\ mol^{-1}} = -2.303R\left(\frac{\mathrm{d}(\log D)}{\mathrm{d}(1/T)}\right)$$

where the slope of the log D *versus* $1/T$ plot corresponds to the heat released or absorbed during complex formation. From linear regression of these plots (Fig. S1a), the calculated ΔH_{app} values for ^{241}Am(III) and ^{244}Cm(III) in 1-octanol were −33.57 kJ mol^{-1} and −36.54 kJ mol^{-1}, respectively. These negative enthalpy values confirm that the extraction of both actinides is strongly exothermic, indicating substantial energy release upon formation of the organic-soluble CA-BTP–metal complexes.

Complementary thermodynamic parameters were derived to dissect the driving forces of extraction further. The standard Gibbs free energy change (ΔG, kJ mol^{-1}) was calculated from the equilibrium extraction constant (log K') using:

$$\Delta G,\ \mathrm{kJ \cdot mol^{-1}} = -2.303RT \quad \log \quad K'$$

and the corresponding entropy change (ΔS) was obtained from the Gibbs–Helmholtz relation:

$$\Delta S,\ \mathrm{J\ mol^{-1}\ K^{-1}} = \frac{\Delta H - \Delta G}{T}$$

The ΔG values, calculated using the extraction equilibrium constant (log K'), were found to be −20.32 kJ mol^{-1} for ^{241}Am(III) and −20.80 kJ mol^{-1} for ^{244}Cm(III), indicating that the extraction process is spontaneous under standard conditions. The corresponding entropy changes were determined to be −44.46 J mol^{-1} K^{-1} for ^{241}Am(III) and −52.81 J mol^{-1} K^{-1} for ^{244}Cm(III), suggesting that extraction is accompanied by a decrease in system disorder, consistent with the formation of well-defined and ordered metal–ligand complexes in the organic phase.

Interestingly, the thermodynamic profile in IDA revealed an even more pronounced enthalpic contribution. The enthalpy changes for ^{241}Am(III) and ^{244}Cm(III) extraction were −42.16 and −42.46 kJ mol^{-1}, respectively, more exothermic than in 1-octanol. Despite slightly less negative ΔG values (−19.64 and −20.83 kJ mol^{-1}), the entropy changes were substantially more negative: −75.75 and −72.58 J mol^{-1} K^{-1}, respectively. These results imply that in IDA, complexation leads to a greater loss in configurational entropy, possibly due to stronger solvation effects and increased ordering of the coordination environment. The branched structure and lower polarity of IDA may facilitate tighter packing or reduced solvation shell mobility around the extracted species, stabilising the metal–ligand adducts more effectively.

The consistently negative ΔS values observed in both systems are characteristic of ligand-driven ordering effects. As the trivalent actinides transition from the aqueous phase into the organic phase coordinated with CA-BTP and nitrate anions, the system undergoes significant structural reorganisation, resulting in entropy loss. This behaviour aligns with trends reported for other soft donor ligands such as BTBP and BTPhen, which exhibit strong enthalpic driving forces and ordered coordination geometries.[38]

The thermodynamic data confirm that the extraction of Am(III) and Cm(III) by CA-BTP is spontaneous, strongly exothermic, and predominantly enthalpy-driven. While both diluents support effective complexation, the greater enthalpic gain observed in IDA may contribute to its slightly higher distribution ratios than 1-octanol. Conversely, the higher entropy cost in IDA underscores the need to consider solvent structure and viscosity in optimising extractant-diluent combinations for scalable partitioning flowsheets.[39,40]

The observed higher magnitude of negative enthalpy values in IDA compared to 1-octanol suggests more favourable complexation energetics in the IDA system, which coincides with marginally higher distribution ratios for both Am(III) and Cm(III). While this correlation may point toward a thermodynamically more stable actinide–ligand complex in IDA, it is important to recognise that such differences cannot be solely attributed to enthalpy without considering the diluent's influence on solvation and interfacial phenomena.

Specifically, electronic interactions between the solvent and the metal centre are indirect in alcohol-based diluents, which are non-coordinating and lack strong donor atoms capable of participating in inner-sphere complexation with actinides. Thus, any diluent effect on complex stability arises not from direct coordination but from modulation of solvation thermodynamics, polarity, hydrogen bonding capacity, and microenvironmental structuring around the ligand–metal complex. The more branched and hydrophobic nature of IDA may better accommodate the neutral CA-BTP-actinide–nitrate complex, thereby reducing desolvation energy and favoring enthalpic stabilisation *via* solvation shell reorganisation.

Therefore, while the slightly more exothermic extraction in IDA suggests enhanced complex stability, this is not due to direct electronic interaction between the solvent and the actinide ion, but rather reflects solvent-mediated stabilisation of the complex. This interpretation is consistent with prior studies of BTP-type ligands in alcohol-rich and mixed diluents, where the choice of diluent alters extraction thermodynamics through solvation dynamics rather than through direct bonding with the metal ion.

These findings highlight the importance of thermodynamic profiling in guiding the rational selection of diluent systems for actinide separations and provide critical insight into the nature of CA-BTP-metal complexation under nuclear waste processing conditions.

3.7. Effect of nitrate ion concentration on extraction and back-extraction of ^{241}Am(III) and ^{154}Eu(III)

The influence of nitrate ion concentration on the extraction behaviour of trivalent metal ions by CA-BTP was investigated to evaluate the role of anion coordination in complex stabilisation and selectivity. Using 0.05 M CA-BTP solutions in 1-octanol and isodecanol (IDA), extraction studies were conducted with aqueous feed solutions containing 0.5 M HNO_3 and varying $NaNO_3$ concentrations from 0.5 to 3.5 M. As shown in Fig. 6, the distribution ratios (D_M) of ^{241}Am(III), ^{244}Cm(III), and ^{154}Eu(III) increased progressively with increasing nitrate ion concentration in both diluent systems. This behaviour is consistent with an equilibrium mechanism involving the formation of neutral metal–nitrate–extractant complexes, wherein excess NO_3^- facilitates charge compensation and stabilises the metal–ligand adducts within the organic phase.

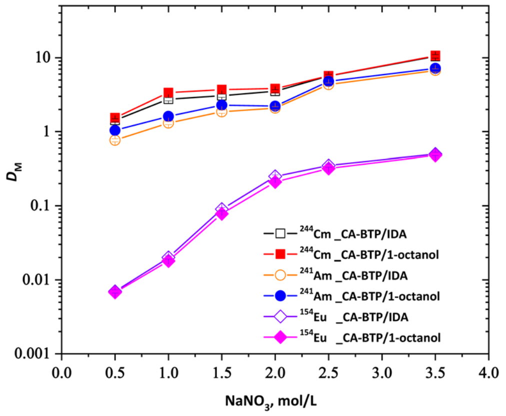

Fig. 6 ^{241}Am, ^{244}Cm and ^{154}Eu distribution ratios a function of $NaNO_3$ concentration. Organic phase: 0.05 M CA-BTP in 1-octanol and IDA. Aqueous phase: 0.5 M HNO_3 with Ln (III)-An(III) rich feed with varying $NaNO_3$ concentration.

The observed nitrate dependence is analogous to extraction trends reported for soft-donor BTP derivatives such as CyMe$_4$-BTP and R-BTP, which also show enhanced extraction efficiency with elevated NO_3^- concentrations. Importantly, no evidence of third-phase formation, emulsion, or precipitation was observed under any condition tested, even at high ionic strength. This highlights the excellent phase stability of CA-BTP systems in both 1-octanol and IDA, representing a key operational advantage over certain phosphine oxide or diglycolamide-based extractants that often suffer from instability under similar conditions.

However, this increased extraction efficiency was accompanied by a decline in selectivity. The separation factor ($SF_{Am/Eu}$) decreased as nitrate concentration increased, owing to a greater proportional increase in Eu(III) extraction relative to Am(III). This trend reflects the enhanced coordination of nitrate anions with Eu(III) at high salt concentrations, which partially offsets the intrinsic soft-donor selectivity of CA-BTP for actinides. Such trade-offs between efficiency and selectivity are well documented for BTP-type extractants and must be carefully optimised in flowsheet design for minor actinide/lanthanide separation processes such as SANEX.

The reversibility of the extraction process was evaluated by performing back-extraction of ^{241}Am(III) from loaded organic phases using 0.01 M HNO_3 as a stripping medium. As shown in Fig. S9, two successive aqueous contacts were sufficient to strip both actinides from both diluent systems completely. This efficient stripping under mild acidity is particularly notable, as similar BTP-based systems (*e.g.*, CyMe$_4$-BTP, R-BTP) often require auxiliary complexants such as DTPA, oxalic acid, or glycolic acid to achieve comparable results. The ability to regenerate the organic phase using only dilute acid simplifies solvent handling, reduces process complexity, and minimises secondary waste generation—key considerations in nuclear waste treatment.

Between the two diluents, IDA demonstrated slightly higher stripping efficiency in each step, likely due to its lower basicity and branched structure, which may destabilise the metal–ligand complex and enhance the thermodynamic driving force for dissociation. However, 1-octanol offered superior phase disengagement kinetics, achieving separation within ∼10 minutes, whereas IDA required ∼30 minutes, with visible interfacial frothing. The longer settling times for IDA likely arise from its higher viscosity and stronger interfacial interactions, which delay aqueous droplet coalescence—an important factor when considering process throughput and engineering design for scale-up.

The influence of feed nitrate concentration on stripping was also examined. Organic phases preloaded with metal ions from nitrate-rich feeds were contacted with 0.01 M HNO_3. As the initial NO_3^- content in the feed increased, a decline in stripping efficiency was observed, attributed to enhanced complex stability due to additional nitrate coordination. Nevertheless, complete recovery of ^{241}Am(III) was still achieved in a single contact for feeds containing up to 2.0 M NO_3^-, affirming the CA-BTP system's robustness under moderately salted conditions. These findings confirm the suitability of CA-BTP for deployment in actinide partitioning schemes such as SANEX and GANEX, where high extraction and facile stripping are essential for operational viability.

3.8. Extraction mechanism and stoichiometry

To elucidate the stoichiometry and complexation mechanism of CA-BTP with trivalent f-elements, slope analyses were conducted by systematically varying CA-BTP concentration (0.005–0.1 M) while keeping the aqueous phase composition constant at 1.0 M NO_3^- and 0.5 M HNO_3. The resulting plots of log D_M *versus* log[CA-BTP] were linear across both diluents (Fig. 7a and b), with slope values indicating the number of ligand molecules involved in complex formation. Under constant nitrate concentration, the extraction equilibrium can be described by the equation,

$$M^{3+}_{(aq)} + 3NO_3^- + n\text{CA}-\text{BTP}_{(org)} \rightleftharpoons [M(\text{CA}-\text{BTP})_n(NO_3)_3]_{(org)}$$
$$\log D_M = n\log[\text{CA}-\text{BTP}] + 3\log[NO_3^-] + \log K'$$

with the slope of the log *D versus* log[CA-BTP] plot provides the apparent stoichiometry (*n*) of CA-BTP molecules involved in complexation.

In 1-octanol, slope values of 2.70 (^{241}Am), 2.62 (^{154}Eu), and 2.65 (^{244}Cm) were obtained. In IDA, the corresponding values were 2.61, 2.53, and 2.54, respectively. These results strongly suggest that a 3 : 1 ligand-to-metal complex, $[M(\text{CA-BTP})_3(NO_3)_3]$, is the predominant species formed under these conditions. Nonetheless, the data also support the possible coexistence of 2 : 1 complex, particularly at lower ligand concentrations or in sterically constrained environments. This dual stoichiometry reflects the structural flexibility of CA-BTP and its ability to adapt to both diluent environments. The tridentate N-donor design allows for cooperative binding and enthalpically favoured chelation of the metal centre.[38] The behaviour mirrors that observed in other BTP-based systems: *n*-Pr-BTP, for example, typically forms a 3 : 1 complex in low-polarity diluents, while CyMe$_4$-BTP, with greater steric hindrance, often favours 2 : 1 coordination under high-acid or constrained conditions.[41]

Interestingly, ^{154}Eu(III) showed minimal extraction even at 1.0 M CA-BTP, with *D* values below 0.1, confirming the ligand's poor affinity for lanthanides under all tested conditions. Furthermore, Eu(III) was easily scrubbed using 1.0 M HNO_3, indicating weak complex formation and confirming the ligand's actinide-selective character. This selectivity is governed by orbital considerations: the nitrogen donors of CA-BTP preferentially stabilise the more spatially extended 5f orbitals of actinides, in accordance with the hard–soft acid–base (HSAB) principle.

Slight deviations from ideal slope values (*i.e.*, 3.0) could stem from a combination of factors, including kinetic limitations at low ligand concentrations, extractant aggregation at higher concentrations, or formation of mixed-ligand species. Regardless, the observed trends affirm that CA-BTP forms stable, extractable complexes with trivalent actinides through a flexible stoichiometry and ligand environment, offering high selectivity and tunable performance based on system conditions. Experiments in 0.5 M HNO_3 with varying $NaNO_3$ concentrations (Fig. 6) were designed to probe the nitrate salting-out effect on Am(III)/Cm(III)/Eu(III) extraction, while 1.0 M HNO_3 (Fig. 7) was selected to simulate conditions closer to HLW. These complementary conditions provide insight into both mechanistic and application-relevant behavior of CA-BTP.

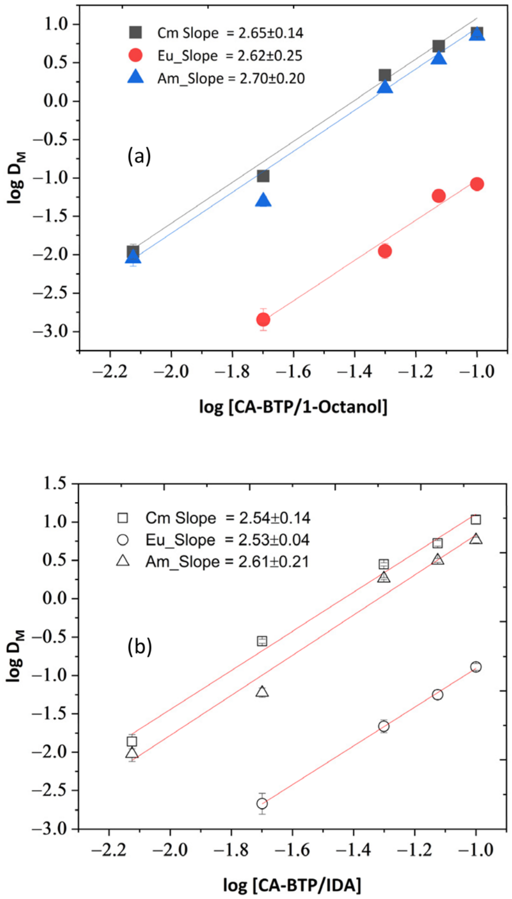

Fig. 7 ^{241}Am, ^{154}Eu and ^{244}Cm distribution ratios as a function of extractant concentration [CA-BTP]. Organic phase: varying CA-BTP in (a) 1-octanol and (b) IDA. Aqueous phase: 1.0 M HNO_3 with Ln (III)-An(III) rich feed.

3.9. Proposed extraction mechanism and ligand–metal interaction pathway

The extraction mechanism of trivalent actinides by CA-BTP has been elucidated through a combination of slope analysis, nitrate dependence studies, and thermodynamic profiling. Experimental log–log plots of distribution ratio (D_M) *versus* CA-BTP concentration yielded slopes ranging from 2.6 to 2.7 for ^{241}Am(III), ^{244}Cm(III), and ^{154}Eu(III) in both 1-octanol and isodecanol (IDA), indicating a predominant ligand-to-metal stoichiometry of 3 : 1. These results support the formation of a neutral complex of the type $[M(CA\text{-}BTP)_3(NO_3)_3]$, wherein each trivalent actinide ion is coordinated by three CA-BTP molecules and charge-compensated by three nitrate ions. Nitrate concentration variation further confirmed this stoichiometry, with extraction efficiency increasing systematically as $NaNO_3$ concentration increased from 0.5 to 3.5 M. The slope of the log *D versus* $\log[NO_3^-]$ plot approached 3.0, indicating the involvement of three nitrate ions in the formation of the extractable complex. These nitrate anions likely participate as inner-sphere ligands, stabilising the neutral species and promoting its solubility in the organic phase.

Thermodynamic analyses revealed that the extraction process is spontaneous and strongly exothermic, with ΔH values ranging from −33 to −42 kJ mol^{-1} and corresponding ΔG values near −20 kJ mol^{-1}. The negative entropy changes observed (−44 to −76 J mol^{-1} K^{-1}) reflect increased order upon complexation, consistent with forming well-defined coordination spheres and structured solvation environments in the organic phase. Notably, slightly more exothermic enthalpy changes in IDA relative to 1-octanol may reflect enhanced solvation compatibility between the diluent and the hydrophobic CA-BTP-metal complex. However, these differences are attributed to solvent-mediated effects rather than direct electronic interactions with the metal ion, as neither 1-octanol nor IDA possesses functional groups capable of coordinating actinide centers. Thus, the diluent's role is limited to modulating the solvation shell, dielectric environment, and interfacial behavior.

Spectroscopic evidence supports this mechanistic model. UV-vis analysis under acidic conditions revealed protonation-induced bathochromic and hyperchromic shifts in the $\pi \rightarrow \pi^*$ transition bands, attributed to changes in the electronic structure of the ligand and stabilisation of the LUMO. These shifts indicate increased electron delocalisation and suggest that protonation of the triazine and pyridyl donors enhances metal-binding capability under mildly acidic conditions. The minimal extraction of ^{154}Eu(III), even at high CA-BTP concentrations, and its complete back-extraction under 1.0 M HNO_3, confirm the ligand's intrinsic selectivity for actinides. This selectivity arises from the preferential stabilisation of the more polarisable 5f orbitals of actinides by the soft nitrogen donors of CA-BTP, per HSAB theory.

3.10. Consistency of CA-BTP synthesis and ^{241}Am(III)/^{154}Eu(III) separation performance

The reproducibility of CA-BTP synthesis was assessed by preparing multiple batches of the ligand at scales ranging from 4 g to 20 g using pyridine-2,6-dicarboxylic acid as the starting material. This alternative precursor, in place of the more expensive pyridine-2,6-dicarbonitrile, offers a cost-effective route to the ligand without compromising the integrity of the final product. Consistency in chemical structure across batches was confirmed by FT-IR spectroscopy (Fig. S1b), where key vibrational bands corresponding to the triazine ring, pyridyl aromatic moieties, and amide functional groups were found to be fully reproducible. The persistent appearance of these characteristic peaks across multiple batches confirmed the retention of the desired coordination architecture essential for metal binding.

To evaluate whether synthetic reproducibility translated into consistent extraction performance, the Am(III)/Eu(III) separation ability of the CA-BTP ligand was tested for each batch. Extractions were performed using 0.10 M CA-BTP dissolved in 1-octanol, contacting a tracer-level aqueous feed containing both ^{241}Am(III) and ^{154}Eu(III). Across all batches, the distribution ratios for ^{241}Am(III) (D_{Am}) were consistently in the range of 6.0–8.5, indicating stable and high extraction efficiency. Correspondingly, the separation factor ($SF_{Am/Eu}$) ranged from 150 to 280, confirming the extractant's reliable selectivity for trivalent actinides over lanthanides under standardised operating conditions (Fig. 8).

To further enhance the selectivity and reduce any trace co-extraction of Eu(III), a mild post-extraction scrubbing step was applied using 1.0 M HNO_3. This acid scrub effectively reduced the residual Eu(III) content in the organic phase, elevating $SF_{Am/Eu}$ to values between 300 and 600, depending on batch purity and extent of extractant purification. Spectral and radiometric analyses confirmed near-complete removal of ^{154}Eu(III), with measured concentrations falling below the minimum detection limit based on a minimum detectable activity (MDA) of 4.5×10^{-4} mCi L^{-1} (Fig. S10a–c). The success of the scrubbing step highlights the tunability and robustness of the CA-BTP system, wherein high selectivity can be further enhanced post-extraction without requiring complex stripping agents or harsh conditions.

The findings establish that CA-BTP can be synthesised reproducibly and cost-effectively without compromising structural fidelity or separation performance. The consistency in chemical identity and extraction behaviour across multiple batches affirms the ligand's potential for application in minor actinide partitioning processes and supports its further development toward process-scale deployment in nuclear waste remediation schemes.

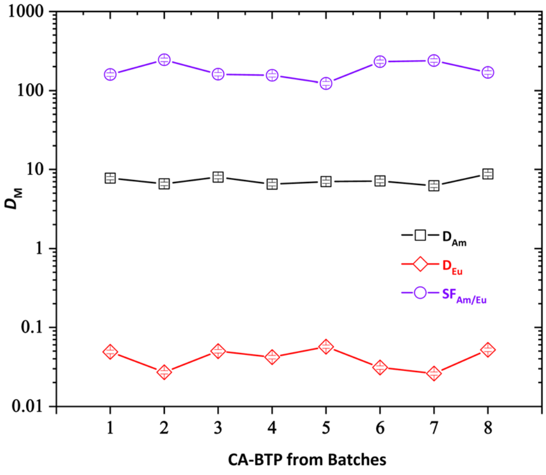

Fig. 8 Distribution ratio and $SF_{Am/Eu}$ of ^{241}Am, ^{154}Eu in 0.1M CA-BTP/1-octanol (CA-BTP synthesised in different batches).

4. Conclusions

A camphorquinone-derived bis-triazinylpyridine (CA-BTP) ligand was successfully synthesised, purified, and evaluated as a soft-donor extractant for the selective separation of trivalent minor actinides from nitric acid media representative of high-level liquid waste (HLW). Structural confirmation of the purified ligand was achieved through FT-IR, ^{1}H NMR, and mass spectrometry, with thermogravimetric and DSC analyses confirming thermal stability. The ligand demonstrated high solubility and acid-phase compatibility in alcohol-based diluents such as 1-octanol and isodecanol (IDA), with no phase separation or emulsification observed up to 2.0 M HNO_3. Acid uptake studies confirmed low proton affinity and high resistance to acid-induced degradation, while UV-vis spectroscopy revealed protonation-induced electronic changes that may enhance coordination behaviour under mildly acidic conditions.

Extraction studies with ^{241}Am(III) and ^{154}Eu(III) revealed that only the chromatographically purified CA-BTP fractions (60–100% EA/PE) exhibited strong actinide uptake with exceptional selectivity over lanthanides. The ligand showed consistent extraction performance across batches, with distribution ratios for Am(III) ranging from 6.0 to 8.5 and separation factors ($SF_{Am/Eu}$) exceeding 150. Mechanistic studies revealed the formation of predominantly 3 : 1 ligand-to-metal complexes of the type $[M(CA\text{-}BTP)_3(NO_3)_3]$, stabilised by inner-sphere nitrate coordination and multidentate N-donor chelation. Slope and nitrate-dependence analyses confirmed this stoichiometry, while thermodynamic profiling demonstrated that extraction is spontaneous, strongly exothermic, and enthalpy-driven in both 1-octanol and IDA. Slightly higher enthalpic stabilisation in IDA suggests improved solvation of the neutral actinide complex, although electronic solvent–metal interactions are not implicated in complex formation.

Back-extraction studies further confirmed that Am(III) and Cm(III) can be quantitatively stripped from the organic phase using only 0.01 M HNO_3, with no requirement for auxiliary stripping agents. Post-extraction scrubbing with 1.0 M HNO_3 efficiently eliminated residual Eu(III), enhancing the selectivity to values exceeding 600. Finally, batch-to-batch reproducibility in both synthesis and separation performance was confirmed, validating the robustness and scalability of the ligand preparation route.

Overall, CA-BTP combines high chemical selectivity, acid resistance, tunable thermodynamic behaviour, and operational simplicity in alcohol-based diluents. These features make it a promising candidate for next-generation minor actinide partitioning systems under HLW-relevant conditions. Further studies on radiolytic stability, process integration, and scale-up feasibility are warranted to support its deployment in advanced nuclear fuel cycle applications.

Author contributions

KA: methodology, investigation, validation, writing – original draft; SJ: conceptualisation, supervision, writing – review & editing; SG: supervision & review; SS: supervision & resources. GSR: project administration.

Conflicts of interest

There are no conflicts to declare.

Data availability

The data supporting this article have been included as part of the supplementary information (SI). The supplementary information provides detailed characterization data and experimental validation supporting the synthesis and evaluation of CA-BTP. This includes FT-IR, ^{1}H-NMR, and mass spectra of intermediates and chromatographic fractions, solvent compatibility and stability photographs, and systematic studies on acid uptake behavior in various diluent systems. Distribution ratio measurements, temperature dependence, and back-extraction experiments for Am(III) and Cm(III) are also presented, alongside gamma-ray spectra of extraction and scrubbing steps. Additionally, the compositions of simulated high-level liquid waste and physicochemical properties of diluents and solvent systems are tabulated. See DOI: **https://doi.org/10.1039/d5ra05245a**.

Acknowledgements

The authors thank the Laboratory officials, WIP-INRPK-NRB, for their timely support and encouragement. In addition, the authors thank Shri K.K. Nandy, Supdt., TSS, WMF, for the IFT analysis.

References

1 P. Zsabka, A. Wilden, K. Van Hecke, G. Modolo, M. Verwerft and T. Cardinaels, *J. Nucl. Mater.*, 2023, **581**, 154445.
2 L. Xu, X. Yang, A. Zhang, C. Xu and C. Xiao, *Coord. Chem. Rev.*, 2023, **496**, 215404.
3 K. Kiegiel, D. Chmielewska-Śmietanko, I. Herdzik-Koniecko, A. Miśkiewicz, T. Smoliński, M. Rogowski, A. Ntang, N. K. Rotich, K. Madaj and A. G. Chmielewski, *Energies*, 2025, **18**, 622.
4 T. Fukasawa, A. Suzuki, Y. Endo, Y. Inagaki, T. Arima, Y. Muroya, K. Endo, D. Watanabe, T. Matsumura, K. Ishii and J. Yamashita, *J. Nucl. Sci. Technol.*, 2024, **61**, 307–317.
5 T. A. Kurniawan, M. H. D. Othman, D. Singh, R. Avtar, G. H. Hwang, T. Setiadi and W. hung Lo, *Ann. Nucl. Energy*, 2022, **166**, 108736.
6 P. Tejaswini, T. Aparna Naguraj, M. Shaik, P. Brindha Devi, Transmutation and Advanced Fuel Cycle: A Future Prospect for Nuclear Waste Reduction, in *Radioactive Pollutant, Environmental Science and Engineering*, ed. N. Kumar, Springer, Cham, 2025, pp. 263–286.
7 J. Kopecky, J.-C. Sublet, J. A. Simpson, R. A. Forrest and D. Nierop, *Atlas of Neutron Capture Cross Sections*, 1997.
8 B. Christiansen, C. Apostolidis, R. Carlos, O. Courson, J. P. Glatz, R. Malmbeck, G. Pagliosa, K. Römer and D. Serrano-Purroy, *Radiochim. Acta*, 2004, **92**, 475–480.

9 B. Christiansen, C. Apostolidis, R. Carlos, O. Courson, J.-P. Glatz, R. Malmbeck, G. Pagliosa, K. Römer and D. Serrano-Purroy, *Radiochim. Acta*, 2004, **92**, 475–480.
10 R. Taylor, G. Mathers and A. Banford, *Prog. Nucl. Energy*, 2023, **164**, 104837.
11 S. Cotton, *Lanthanide and Actinide Chemistry*, John Wiley & Sons, Hoboken, NJ, USA, 2nd edn, 2024.
12 E. A. Konopkina, A. V. Gopin, A. S. Pozdeev, M. G. Chernysheva, P. Kalle, E. A. Pavlova, S. N. Kalmykov, V. G. Petrov, N. E. Borisova, A. A. Guda and P. I. Matveev, *Phys. Chem. Chem. Phys.*, 2024, **26**, 2548–2559.
13 P. Distler, M. Mindova, J. Sebesta, B. Gruner, D. Bavol, R. J. M. Egberink, W. Verboom, V. A. Babain and J. John, *ACS Omega*, 2021, **6**, 26416–26427.
14 A. Bhattacharyya and P. K. Mohapatra, *Radiochim. Acta*, 2019, **107**, 931–949.
15 A. Geist, C. Hill, G. Modolo, M. R. St. J. Foreman, M. Weigl, K. Gompper and M. J. Hudson, *Solvent Extraction and Ion Exchange*, 2006, vol. 24, pp. 463–483.
16 X. Yang, D. Fang, L. Chen, Y. Liu, S. Wang, L. Xu, A. Zhang, J. Su, C. Xu and C. Xiao, *JACS Au*, 2024, **4**, 4744–4756.
17 Z. Wang, J. Wang, S. Ding, Y. Liu, L. Zhang, L. Song, Z. Chen, X. Yang and X. Wang, *Sep. Purif. Technol.*, 2019, **210**, 107–116.
18 S. Lin Zhang, L. Yu, Y. Liu, J. F. Gallagher, H. Xin Hao, Y. Qiang Wan, Z. Peng Wang, J. Li Wang, T. Hong Yan, W. Qun Shi and P. Mocilac, *Sep. Purif. Technol.*, 2025, **357**, 130011.
19 S. Trumm, A. Geist, P. J. Panak and T. Fanghänel, *Solvent Extraction and Ion Exchange*, 2011, vol. 29, pp. 213–229.
20 A. Geist and P. J. Panak, *Solvent Extraction and Ion Exchange*, 2021, vol. 39, pp. 128–151.
21 K. Anshul, J. Selvakumar, S. Srinivasan, G. Suneel, N. R. Jawahar, J. K. Gayen and K. V. Ravi, *Sep. Sci. Technol.*, 2023, **58**, 2631–2640.
22 D. Nair, P. Gireesan, D. Banerjee, R. K. Mishra, S. Kumar and S. Manohar, *J. Radioanal. Nucl. Chem.*, 2022, **331**, 5557–5567.
23 K. N. Tevepaugh, J. D. Carrick, S. Tai, J. G. Coonce, L. H. Delmau and D. D. Ensor, *Solvent Extraction and Ion Exchange*, 2016, vol. 34, pp. 13–25.
24 S. Ning, Q. Zou, X. Wang, R. Liu, Y. Wei, Y. Zhao and Y. Ding, *J. Radioanal. Nucl. Chem.*, 2016, **307**, 993–999.
25 S. Liu, D. Brunel, K. Sun, Y. Xu, F. Morlet-Savary, B. Graff, P. Xiao, F. Dumur and J. Lalevée, *Polym. Chem.*, 2020, **11**, 3551–3556.
26 S. V. Asmussen and C. I. Vallo, *Polym. Degrad. Stab.*, 2017, **137**, 244–250.
27 H. Rahimi, R. Hosseinzadeh and M. Tajbakhsh, *J. Photochem. Photobiol., A*, 2021, **407**, 113049.
28 P. J. Panak and A. Geist, *Chem. Rev.*, 2013, **113**, 1199–1236.
29 Z. Zhu, X. Wang, H. Yu, W. Zhou, Y. Wang, J. Han and F. Guo, *Cryst. Growth Des.*, 2023, **23**, 1455–1465.
30 N. E. Braml, L. Stegbauer, B. V. Lotsch and W. Schnick, *Chem.–Eur. J*, 2015, **21**, 7866–7873.
31 J. Dong, S. Chen, H. Li, F. Zhao and K. Xu, *FirePhysChem*, 2022, **2**, 207–213.
32 M. Altarawneh and L. Ali, *Energy Fuels*, 2024, **38**, 21735–21792.
33 P. Zsabka, K. Van Hecke, L. Adriaensen, A. Wilden, G. Modolo, M. Verwerft, K. Binnemans and T. Cardinaels, *RSC Adv.*, 2021, **11**, 6014–6021.
34 A. Geist, *Solvent Extraction and Ion Exchange*, 2010, vol. 28, pp. 596–607.
35 S. H. Hasan and J. P. Shukla, *J. Radioanal. Nucl. Chem.*, 2003, **258**, 563–573.
36 J. N. Sharma, R. Ruhela, K. N. Harindaran, S. L. Mishra, S. K. Tangri and A. K. Suri, *J. Radioanal. Nucl. Chem.*, 2008, **278**, 173–177.
37 R. Ruhela, J. N. Sharma, B. S. Tomar, V. C. Adya, T. K. Sheshgiri, R. C. Hubli and A. K. Suri, *Sep. Sci. Technol.*, 2011, **46**, 965–971.
38 E. Löfström-Engdahl, E. Aneheim, C. Ekberg, M. Foreman and G. Skarnemark, *Sep. Sci. Technol.*, 2014, **49**, 2060–2065.
39 J. Selvakumar, S. Srinivasan, G. Suneel, S. Bera, C. V. S. Brahmananda Rao, G. S. Rao and J. K. Gayen, *ACS Omega*, 2025, **10**, 8911–8921.
40 S. Jayaparakasam, S. Gattu, S. Maity, K. Anshul, P. A. Nishad, A. Bhaskarapillai, S. Srinivasan, G. Srinivasa Rao, J. K. Gayen and T. V. K. Mohan, *Sep. Sci. Technol.*, 2025, 1–17.
41 A. Bremer, U. Müllich, A. Geist and P. J. Panak, *New J. Chem.*, 2015, **39**, 1330–1338.